Enhancement of Linear Antenna Arrays through an Innovative *QCTO-SI* Method: Preliminary Assessment

M. Salucci, G. Oliveri, N. Anselmi, G. Gottardi, and A. Massa

Abstract

In this work, an innovative Material-by-Design (*MbD*) methodology is proposed to improve the radiation features of a linear active electronically-scanned array (*AESA*) without increasing the number of elements nor requiring the re-design of the radiators and/or feeding network. The quasi-conformal transformation optics (*QCTO*) approach is exploited to design an enhancing meta-material lens that is able to focus the radiated field of the original antenna. Moreover, a source inversion (*SI*) strategy is adopted to properly set the array excitations in order to match the radiation characteristics of significantly larger apertures. Some preliminary numerical results are reported and discussed.

1 Problem Formulation and Definitions

1.1 Goal

Let be given a physical array made of N elements with spacing $d = \frac{\lambda}{2}$. Our goal is to enhance its radiation properties by properly synthesizing a metamaterial lens that covers it. Such an enhancement can be obtained in principle by

1. Increasing the overall aperture / number of elements of the array;
2. Increasing the radiation characteristics of the radiating elements.

In this report, the first option is investigated, and the lens will be synthesized in order to make the radiation characteristics of the original array similar to those of a larger array (i.e., made of mode equi-spaced elements) in free-space.

1.2 Transformation Description

The transformation involves two spatial domains. In this report, the first domain is called "virtual domain" or "virtual space" while the other one is referred to as "physical domain" or "physical space". In addition, the terms "virtual" and "physical" are used to describe entities in virtual and physical spaces respectively. The rectangular coordinate system in virtual space is labeled as (x', y', z') whereas in the physical space the labels (x, y, z) are used.

If the transformation from (x', y', z') to (x, y, z) is defined as:

$$(x, y, z) = \Gamma\left(x', y', z'\right) \tag{1}$$

$$x = x\left(x', y', z'\right) \tag{2}$$

$$y = y\left(x', y', z'\right) \tag{3}$$

$$z = z\left(x', y', z'\right) \tag{4}$$

the Jacobian matrix of the transformation $\underline{\underline{\Lambda}}$ will be:

$$\underline{\underline{\Lambda}} = \begin{bmatrix} \frac{\partial x}{\partial x'} & \frac{\partial x}{\partial y'} & \frac{\partial x}{\partial z'} \\ \frac{\partial y}{\partial x'} & \frac{\partial y}{\partial y'} & \frac{\partial y}{\partial z'} \\ \frac{\partial z}{\partial x'} & \frac{\partial z}{\partial y'} & \frac{\partial z}{\partial z'} \end{bmatrix}. \tag{5}$$

For the inverse transformation, i.e. (x, y, z) to (x', y', z'),

$$(x', y', z') = \Gamma'\left(x, y, z\right) \tag{6}$$

$$x' = x'(x, y, z) \tag{7}$$

$$y' = y'(x, y, z) \tag{8}$$

$$z' = z'(x, y, z) \tag{9}$$

the corresponding Jacobian matrix will be

$$\underline{\underline{\Lambda}}' = \begin{bmatrix} \frac{\partial x'}{\partial x} & \frac{\partial x'}{\partial y} & \frac{\partial x'}{\partial z} \\ \frac{\partial y'}{\partial x} & \frac{\partial y'}{\partial y} & \frac{\partial y'}{\partial z} \\ \frac{\partial z'}{\partial x} & \frac{\partial z'}{\partial y} & \frac{\partial z'}{\partial z} \end{bmatrix}. \tag{10}$$

and the following relations can be established.

$$\underline{\underline{\Lambda}}' = \underline{\underline{\Lambda}}^{-1} \tag{11}$$

$$det\left(\underline{\underline{\Lambda}}'\right) = \frac{1}{det\left(\underline{\underline{\Lambda}}\right)} \tag{12}$$

If $\underline{\underline{\varepsilon}}'$ and $\underline{\underline{\mu}}'$ represent relative permittivity and relative permeability tensors in the virtual medium respectively,

$$\underline{\underline{\varepsilon}}' = \begin{bmatrix} \varepsilon'_{xx} & \varepsilon'_{xy} & \varepsilon'_{xz} \\ \varepsilon'_{yx} & \varepsilon'_{yy} & \varepsilon'_{yz} \\ \varepsilon'_{zx} & \varepsilon'_{zy} & \varepsilon'_{zz} \end{bmatrix} \tag{13}$$

$$\underline{\underline{\mu}}' = \begin{bmatrix} \mu'_{xx} & \mu'_{xy} & \mu'_{xz} \\ \mu'_{yx} & \mu'_{yy} & \mu'_{yz} \\ \mu'_{zx} & \mu'_{zy} & \mu'_{zz} \end{bmatrix} \tag{14}$$

the corresponding relative permittivity and relative permeability tensors in physical space can be computed as follows:

$$\underline{\underline{\varepsilon}} = \frac{\underline{\underline{\Lambda}}\,\underline{\underline{\varepsilon}}'\,\underline{\underline{\Lambda}}^T}{det\left(\underline{\underline{\Lambda}}\right)} \tag{15}$$

$$\underline{\underline{\mu}} = \frac{\underline{\underline{\Lambda}}\,\underline{\underline{\mu}}'\,\underline{\underline{\Lambda}}^T}{det\left(\underline{\underline{\Lambda}}\right)}. \tag{16}$$

If there is a source with current I' and current density $\underline{J}'$ in virtual space its corresponding image in the physical space can be computed as

$$\underline{J} = \frac{\underline{\underline{\Lambda}}\,\underline{J}'}{det\left(\underline{\underline{\Lambda}}\right)}. \tag{17}$$

$$I = I'. \tag{18}$$

1.3 Isotropic Approximation

An isotropic approximation can be made on the permittivity and permeability of the medium (Lens) in the physical space under the following assumptions:

- TE or TM mode of propagation.
- Grid lines in virtual space are "near" orthogonal which results in a near-isotropic medium in virtual space.

Under such assumptions, permittivity and permeability in physical space will be simplified as:

- For TE mode of propagation:
  - Approximate Isotropic permeability: $\underline{\underline{\mu}}^{approx.} = \mu^{approx.}\mathbb{I}$;
  - Constant Approximate permittivity: $\underline{\underline{\varepsilon}}^{approx.} = \mathbb{I}$;
- For TM mode of propagation:
  - Approximate Isotropic permittivity: $\underline{\underline{\varepsilon}}^{approx.} = \varepsilon^{approx.}\mathbb{I}$;
  - Constant Approximate permeability: $\underline{\underline{\mu}}^{approx.} = \mathbb{I}$;

where $\mathbb{I}$ is a 3×3 identity matrix, $\varepsilon^{approx.}$ and $\mu^{approx.}$ are computed by ratio of areas of virtual and physical transformation grid cells. More specifically, for a given unit cell in the physical space, if its area is approximated by $A^{physical} = \Delta x \Delta y$, where Δx and Δy are changes in x and y between its opposite corners, and similarly if the area of the image of this unit cell in virtual space can be approximated by $A^{virtual} = \Delta x' \Delta y'$, the approximate permittivity or permeability of the unit cell is computed as: $\frac{A^{virtual}}{A^{physical}} = \frac{\Delta x' \Delta y'}{\Delta x \Delta y}$.

- For TE mode of propagation:

$$\mu^{approx.} = \frac{A^{virtual}}{A^{physical}} = \frac{\Delta x' \Delta y'}{\Delta x \Delta y} \tag{19}$$

- For TM mode of propagation:

$$\varepsilon^{approx.} = \frac{A^{virtual}}{A^{physical}} = \frac{\Delta x' \Delta y'}{\Delta x \Delta y} \tag{20}$$

1.4 Transformation Grid Orthogonality (χ)

Since the orthogonality of the transformation grid is the basis for isotropic approximation, it is quantified as follows. Figure 1 shows a sample grid intersection in the complex plane $\gamma = x + jy$.

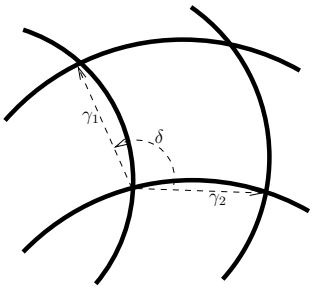

Figure 1: Description of grid orthogonality measure: A sample unit cell of a grid in the complex plane

Referring to Figure 1, and using Euler's notation, $\gamma_1 = |\gamma_1| e^{j[arg(\gamma_1)]}$, $\gamma_2 = |\gamma_2| e^{j[arg(\gamma_2)]}$, where γ_1 and γ_2 are vectors forming adjacent sides of the unit cell. The internal angle δ can be computed as

$$\delta = arg(\gamma_1) - arg(\gamma_2) = arg\left(\frac{\gamma_1}{\gamma_2}\right).$$

The offset from orthogonality χ can then be evaluated as

$$\chi = \delta - 90. \tag{21}$$

1.5 Field Matching Error (ξ)

The error between a given field distribution E and a reference field distribution E_{ref} sampled at U and V points in the x and y directions respectively (i.e $x_u \in \{x_1, \cdots, x_U\}$, $y_v \in \{y_1, \cdots, y_V\}$) is evaluated as:

$$\xi = \frac{\sum_{u=1}^{U} \sum_{v=1,(x_u,y_v)\notin\Theta}^{V} |E_{ref}(x_u, y_v) - E(x_u, y_v)|}{\sum_{u=1}^{U} \sum_{v=1,(x_u,y_v)\notin\Theta}^{V} |E_{ref}(x_u, y_v)|} \tag{22}$$

where Θ represents an area excluded from the evaluation. This expression is typically used to evaluate the difference between fields radiated from a reference virtual array and an array enhanced by metamaterial lens, where the comparison is made outside the lens region (i.e., Θ is the boundary of the synthesized lens).

1.6 Anisotropy Measures

- Maximum lens permittivity

$$\max\left\{\underline{\underline{\varepsilon}}\right\} = \max_{\mathbf{r}\in\Omega}\left\{\varepsilon_{pq}(\mathbf{r}); p, q \in \{1, 2, 3\}\right\}$$

- Minimum lens permittivity

$$\min\left\{\underline{\underline{\varepsilon}}\right\} = \min_{\mathbf{r}\in\Omega}\left\{\varepsilon_{pq}(\mathbf{r}); p, q \in \{1, 2, 3\}\right\}$$

- Average fractional anisotropy

$$\alpha_F = \frac{1}{area(\Omega)} \int_{\mathbf{r}\in\Omega} \sqrt{\frac{3\sum_{i=1}^{3}\left[\sigma_i(\mathbf{r}) - \sigma_{ave}(\mathbf{r})\right]^2}{2\sum_{i=1}^{3}\left[\sigma_i(\mathbf{r})\right]^2}} d\mathbf{r}$$

- Average relative anisotropy

$$\alpha_R = \frac{1}{area(\Omega)} \int_{\mathbf{r}\in\Omega} \sqrt{\frac{\sum_{i=1}^{3}\left[\sigma_i(\mathbf{r}) - \sigma_{ave}(\mathbf{r})\right]^2}{3\sigma_{ave}(\mathbf{r})}} d\mathbf{r}$$

Where

- $\sigma_i(\mathbf{r})$, $i = 1, ..., 3$ are the eigenvalues of the permittivity tensor $\underline{\underline{\varepsilon}}(\mathbf{r})$;
- $\sigma_{ave}(\mathbf{r}) = \frac{\sum_{i=1}^{3} \sigma_i(\mathbf{r})}{3}$ is the average of the eigenvalues;
- Ω is the external perimeter of the lens.

1.7 Directivity

The directivity is defined as

$$D(\theta, \phi) = \frac{4\pi F(\theta, \phi)}{\int_0^{2\pi} \int_0^{\pi} F(\theta, \phi) \sin(\theta) \, d\theta d\phi} \tag{23}$$

where

$$F(\theta, \phi) = |E(\theta, \phi)|^2 \tag{24}$$

is the square of the absolute value of the far-field electric field. Accordingly, the maximum directivity is defined as

$$D_{\max} = \frac{4\pi \max_{(\theta,\phi)} \{F(\theta, \phi)\}}{\int_0^{2\pi} \int_0^{\pi} F(\theta, \phi) \sin(\theta) \, d\theta d\phi} \tag{25}$$

Note that $4\pi = \int_0^{2\pi} \int_0^{\pi} \sin(\theta) \, d\theta d\phi$ is the solid angle. Under the hypothesis that

- The array elements are displaced on the (x, y) plane;
- The array elements are modeled as infinite line sources oriented along the z axis;
- The pattern is computed on the (x, y) plane, i.e., by considering $\theta = \frac{\pi}{2}$ and $0 \leq \phi \leq 2\pi$;

we have that the directivity is computed as

$$D\left(\theta = \frac{\pi}{2}, \phi\right) = \frac{2\pi F\left(\theta = \frac{\pi}{2}, \phi\right)}{\int_0^{2\pi} F\left(\theta = \frac{\pi}{2}, \phi\right) d\phi} \tag{26}$$

and

$$D_{\max} = \frac{2\pi \max_{\phi} \left\{F\left(\theta = \frac{\pi}{2}, \phi\right)\right\}}{\int_0^{2\pi} F\left(\theta = \frac{\pi}{2}, \phi\right) d\phi} \tag{27}$$

where $2\pi = \int_0^{2\pi} d\phi$, and the integral at the denominator is approximated as

$$\int_0^{2\pi} F\left(\theta = \frac{\pi}{2}, \phi\right) d\phi \cong \sum_{q=1}^{Q-1} F\left(\theta = \frac{\pi}{2}, \phi = \phi_q\right) \Delta\phi \tag{28}$$

where Q is the number of pattern samples and $\Delta\phi = \frac{2\pi}{(Q-1)}$ is the angular step. We then get

$$D_{\max} \cong \frac{2\pi \max_{\phi}\left\{F\left(\theta=\frac{\pi}{2},\phi\right)\right\}}{\frac{2\pi}{(Q-1)}\sum_{q=1}^{Q-1}F\left(\theta=\frac{\pi}{2},\phi=\phi_q\right)} = \frac{\max_{\phi}\left\{F\left(\theta=\frac{\pi}{2},\phi\right)\right\}}{\frac{1}{(Q-1)}\sum_{q=1}^{Q-1}F\left(\theta=\frac{\pi}{2},\phi=\phi_q\right)}. \quad (29)$$

2 Color Legend

Array	Num. Elements	Spacing	Environment	Color
Physical @ Step 1	N	$\lambda/2$	Free-Space	GREY
Virtual @ Step 2	N'	$\lambda/2$	Free-Space	RED
Physical @ Step 2	N'	$< \lambda/2$	Free-Space	GREEN
Physical @ Step 2	N'	$< \lambda/2$	Aniso-Lens	BLUE
Physical @ Step 2	N'	$< \lambda/2$	Iso-Lens	MAGENTA
Physical @ Step 1 + SI	N	$\lambda/2$	Free-Space	ORANGE
Physical @ Step 1 + SI	N	$\lambda/2$	Aniso-Lens	CYAN
Physical @ Step 1 + SI	N	$\lambda/2$	Iso-Lens	BLACK

Table I: Color legend for the different arrays.

3 Test Case # 1 - Triangular Profile, $N = 15$, $N' = 17$

3.1 Step 1: Expanding the physical array ($N = 15$, $L = 7.0$ [λ])

Input Parameters

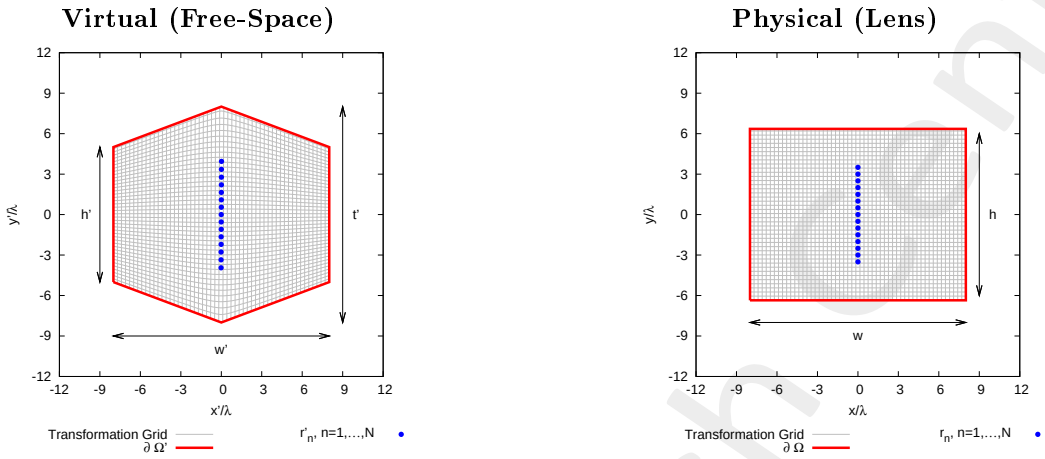

(a) (b)

Figure 2: Transformation regions.

- **Physical Array**
  - Number of elements, spacing, aperture: $N = 15$, $d = \frac{\lambda}{2}$, $L = 7.0$ [λ];
  - Positions: $x_n = 0.0$, $y_n \in [-L/2, L/2]$, $n = 1, ..., N$;
  - Steering angle: $\phi_s = 0.0$ [deg];
  - Excitations: $I_n = 1.0$, $\varphi_n = \frac{-2\pi}{\lambda} y_n sin\,(\phi_s)$; $n = 1, ..., N$;
- **Virtual Geometry**
  - Dimensions: $w' = 16.0$ [λ], $h' = 10.0$ [λ], $t' = 16.0$ [λ];
- **QCTO**
  - Discretization cell dimension: 0.15 [λ] (0.01 [λ] for source mapping);

3.1.1 Results

- Aperture of the virtual array: $L' \simeq 7.88$ [λ];
- Number of equi-spaced elements in L': $N' = round\left(\frac{L'}{0.5} + 1\right) = 17$

3.2 Step 2: Compressing the virtual array ($N' = 17$, $L' = 8.0$ [λ])

Input Parameters

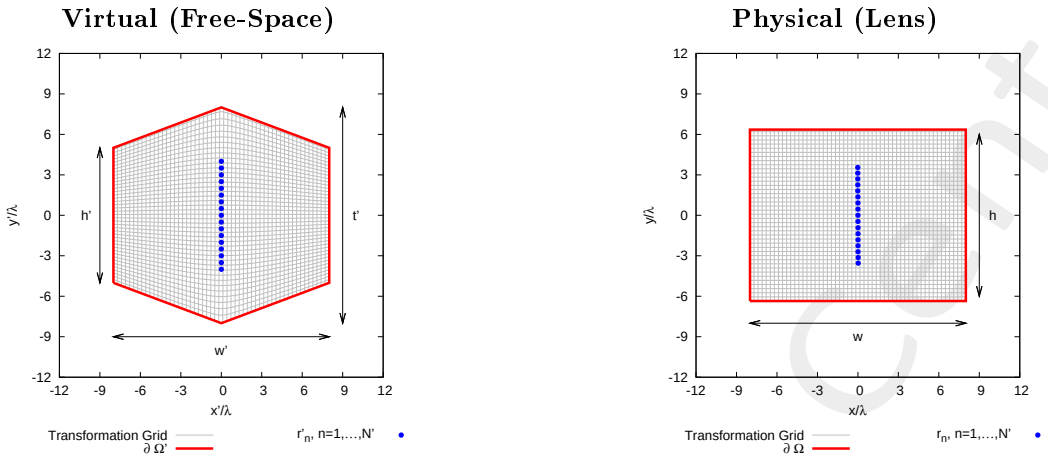

(a) (b)

Figure 3: Transformation regions.

- **Virtual Array**
  - Number of elements, spacing, aperture: $N' = 17$, $d' = \frac{\lambda}{2}$, $L' = 8.0$ [λ];
  - Positions: $x'_n = 0.0$, $y'_n \in [-L'/2, L'/2]$, $n = 1, ..., N'$;
  - Steering angle: $\phi_s = 0.0$ [deg];
  - Excitations: $I'_n = 1.0$, $\varphi'_n = \frac{-2\pi}{\lambda} y_n sin\,(\phi_s)$; $n = 1, ..., N'$;
- **Virtual Geometry:** same of step 1;
- **QCTO:** same of step 1;

3.2.1 Results of the Transformation

Lens Permittivity

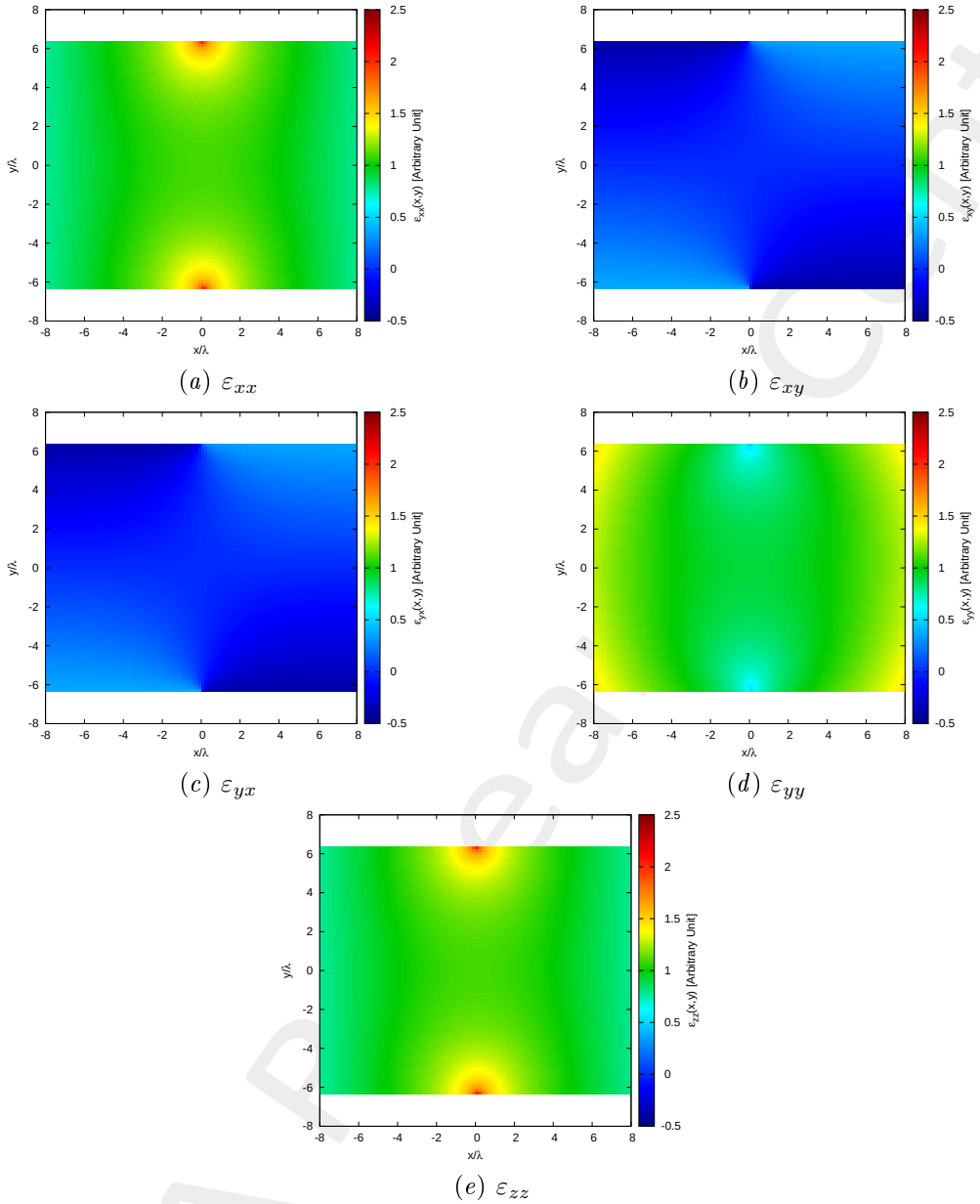

(a) ε_{xx} (b) ε_{xy} (c) ε_{yx} (d) ε_{yy} (e) ε_{zz}

Figure 4: Components of the relative permittivity tensor of the lens.

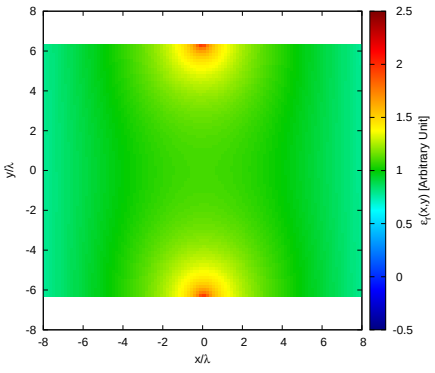

Figure 5: Isotropic approximate permittivity distribution of the lens.

Physical Lens Parameters

Parameter	Value
Height, h [λ]	12.70
Width, w [λ]	16.0
Anisotropic Permittivity Range	$[-0.38, 2.01]$
Isotropic Permittivity Range	$[0.00, 1.95]$

Table II: Transformation statistics. Note that we impose $w = w'$, while h' is internally chosen.

Virtual Grid Orthogonality

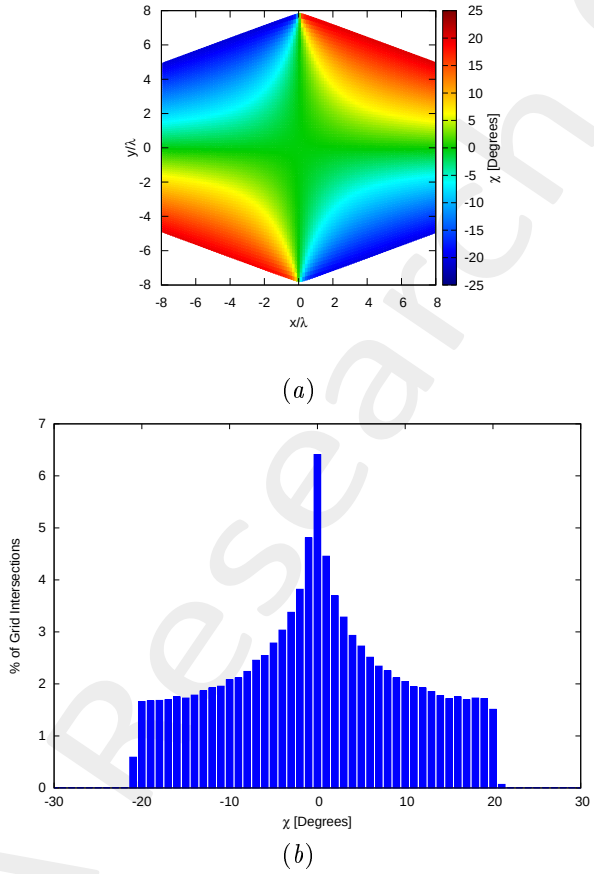

(a)

(b)

Figure 6: Orthogonality of the virtual region.

3.2.2 Near-Field Distributions ($\phi_s = 0$ [deg], $f = 600$ [MHz])

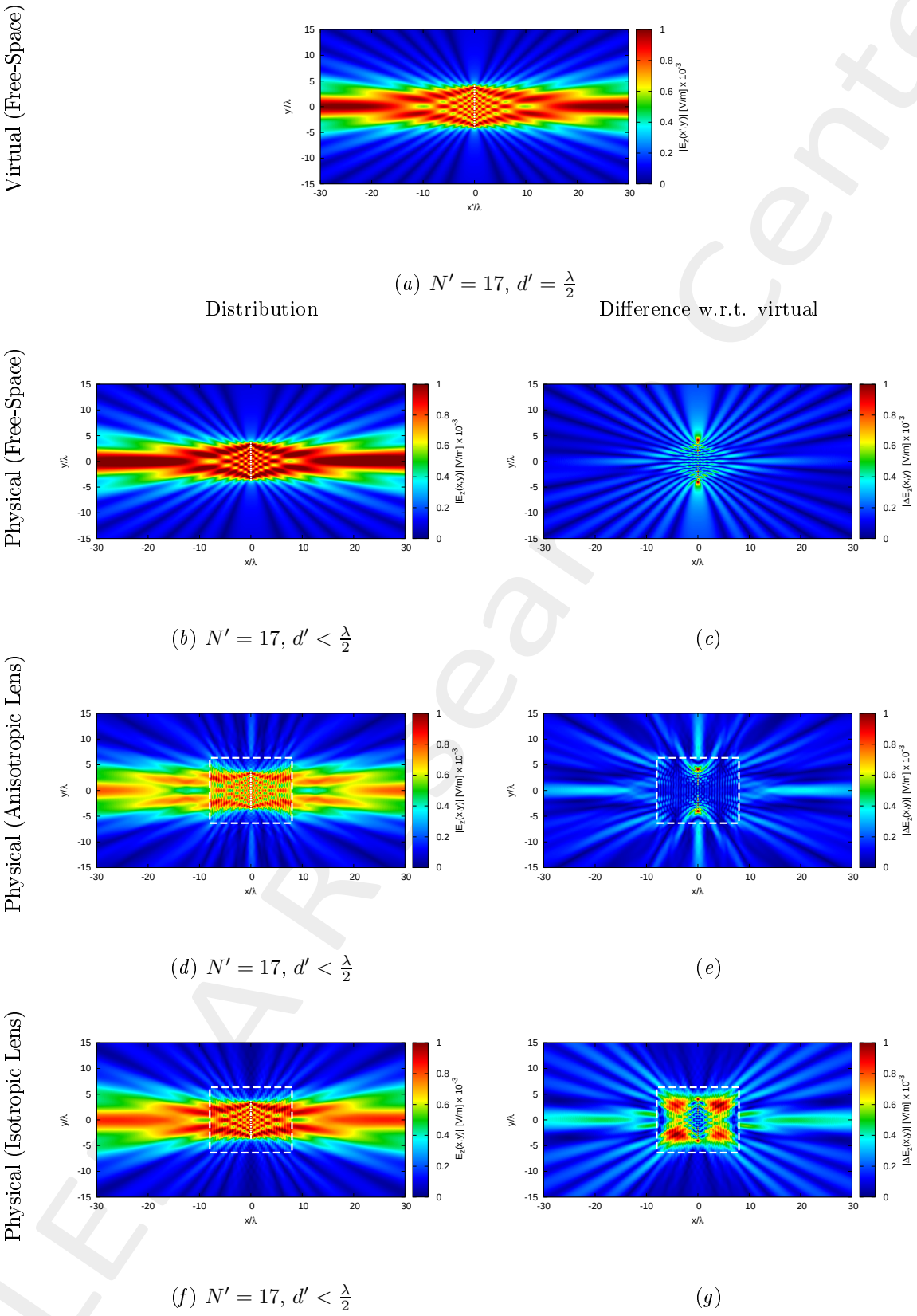

(a) $N' = 17$, $d' = \frac{\lambda}{2}$

(b) $N' = 17$, $d' < \frac{\lambda}{2}$ (c)

(d) $N' = 17$, $d' < \frac{\lambda}{2}$ (e)

(f) $N' = 17$, $d' < \frac{\lambda}{2}$ (g)

Figure 7: Electric field distributions.

3.2.3 Far-Field Patterns ($\phi_s = 0$ [deg], $f = 600$ [MHz])

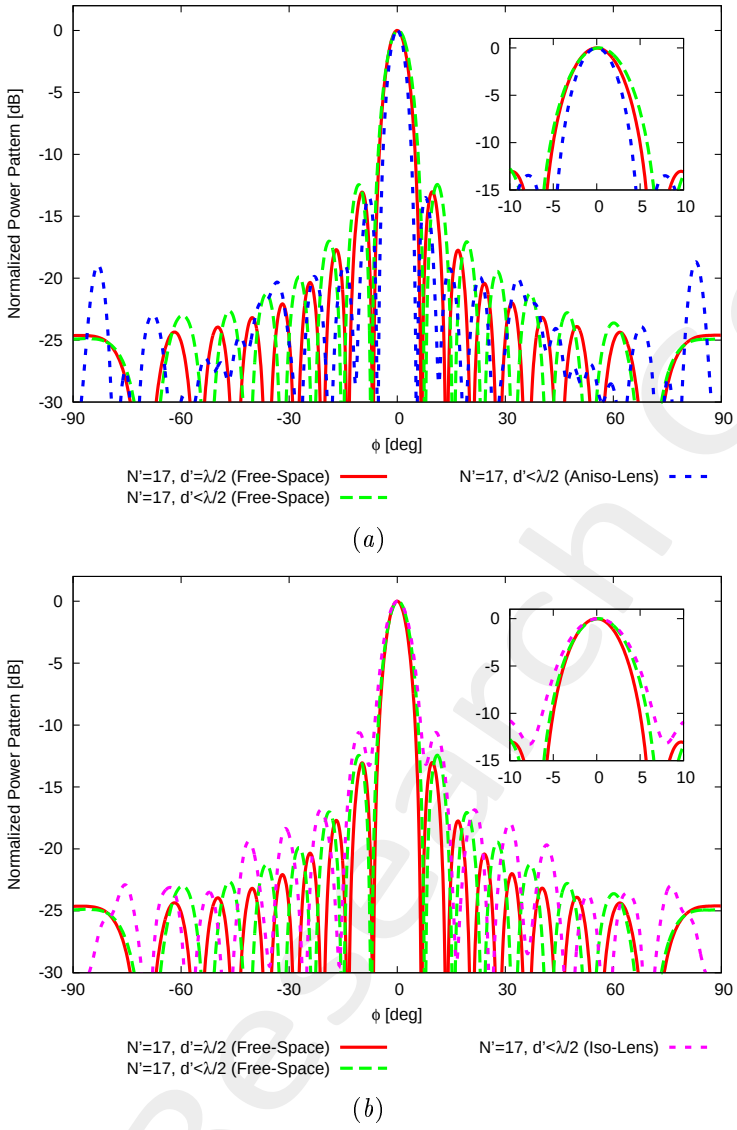

Figure 8: Comparison between normalized power patterns.

3.2.4 Summary ($\phi_s = 0$ [deg], $f = 600$ [MHz])

	Virtual Array	**Physical Array**		
Environment	Free-Space	Free-Space	Aniso-Lens	Iso-Lens
Number of elements	17	17		
Spacing [λ]	0.5	< 0.5		
Aperture [λ]	8.0	7.09		
$SLL[dB]$	13.03	12.43	13.46	10.60
$FNBW$ [deg]	13.60	14.95	10.80	15.76
$3dB$ Beamwidth [deg]	5.98	6.66	4.70	7.45
Matching Error, ξ (w.r.t. virtual, outside lens)	-	4.80×10^{-1}	5.12×10^{-1}	6.49×10^{-1}

Table III: Summary.

3.3 Source Inversion (SI)

Parameters

- Before SI
  - Number of elements: $N' = 17$, $d' < \lambda/2$;
- After SI
  - Number of elements after SI: $N = 15$, $d = \frac{\lambda}{2}$;
  - Aperture: $L = 7.0$;
- Radius of the observation domain: $r_{SI} = 20.0$ [λ];
- Number of field sampling points: $n_{SI} = 1000$.

3.3.1 Results of the SI

Synthesized Excitations ($\phi_s = 0$ [deg], $f = 600$ [MHz])

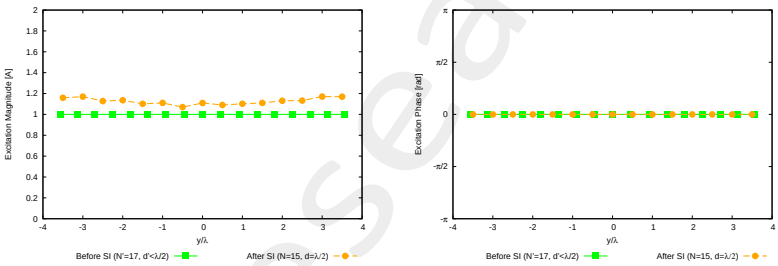

(a) (b)

Figure 9: Excitations of the array ($N = 15$, $d = \frac{\lambda}{2}$) before and after SI.

Check SI: Free-Space Patterns ($\phi_s = 0$ [deg], $f = 600$ [MHz])

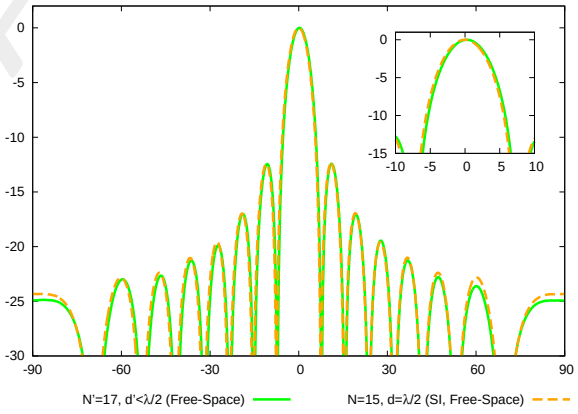

Figure 10: Free-space patterns of reference array and synthesized array after SI.

3.3.2 Near-Field Distribution ($\phi_s = 0$ [deg], $f = 600$ [MHz])

Virtual (Free-Space)

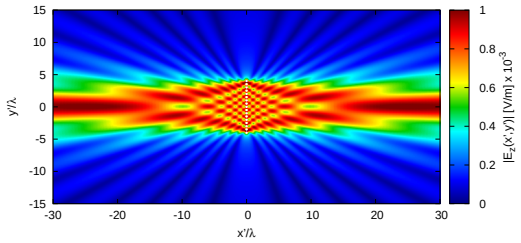

(a) $N' = 17$, $d' = \frac{\lambda}{2}$

Distribution | Difference w.r.t. virtual

Physical (Free-Space)

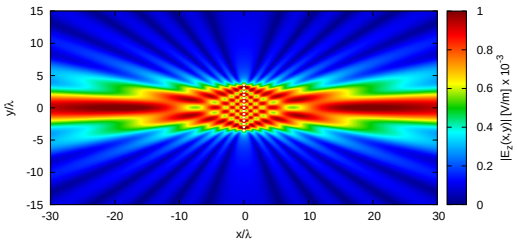

(b) $N = 15$, $d = \frac{\lambda}{2}$, No-SI

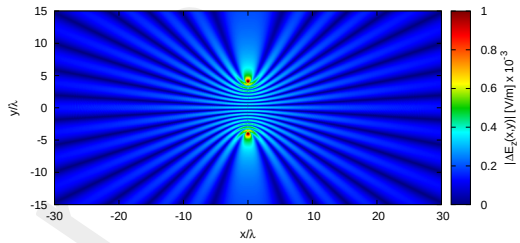

(c)

Physical (Anisotropic Lens)

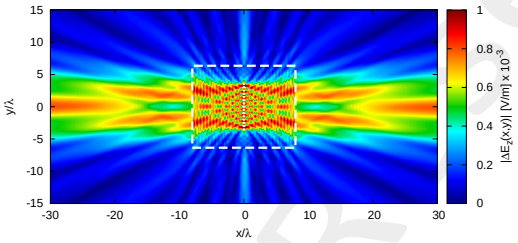

(d) $N = 15$, $d = \frac{\lambda}{2}$, SI

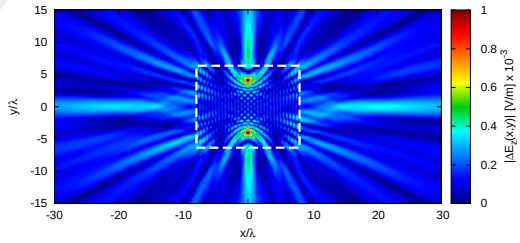

(e)

Physical (Isotropic Lens)

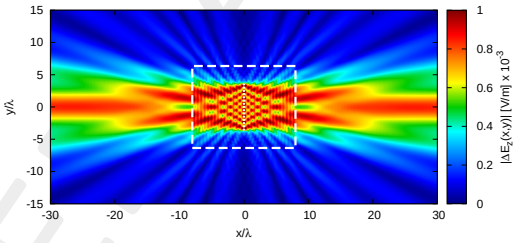

(f) $N = 15$, $d = \frac{\lambda}{2}$, SI

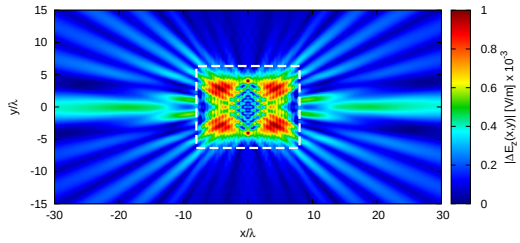

(g)

Figure 11: Electric field distributions.

3.3.3 Far-Field Patterns ($\phi_s = 0$ [deg], $f = 600$ [MHz])

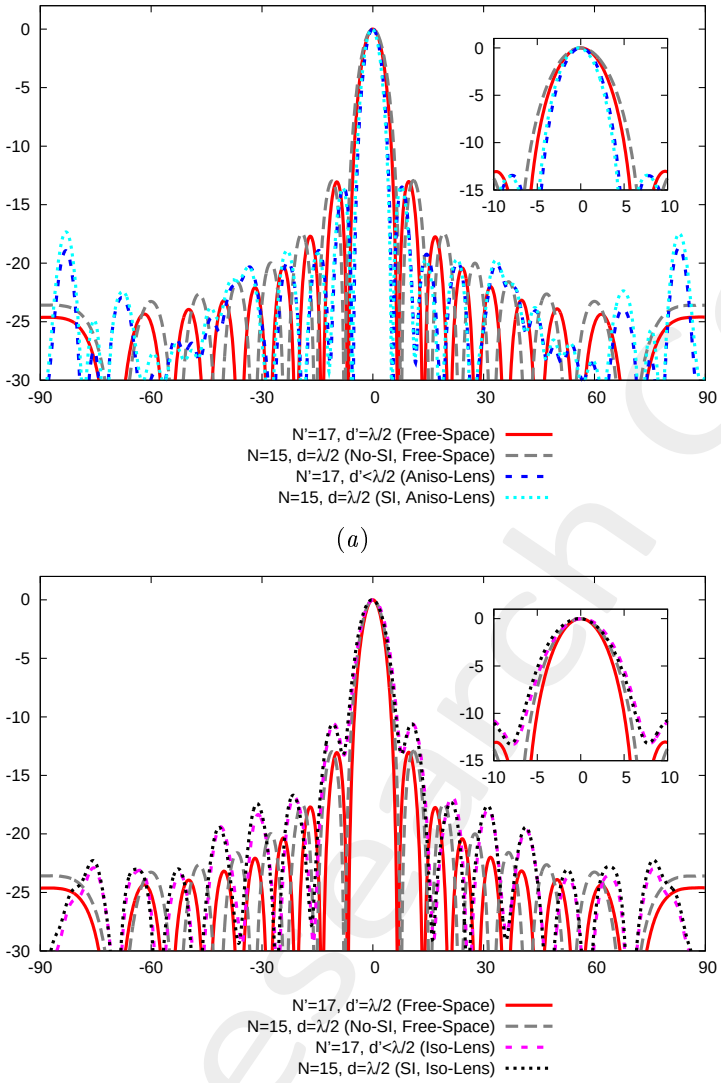

Figure 12: Comparison between normalized power patterns.

3.3.4 Final Summary ($\phi_s = 0$ [deg], $f = 600$ [MHz])

	Virtual Array	**Physical Array**		
Environment	Free-Space	Free-Space (No-SI)	Aniso-Lens (SI)	Iso-Lens (SI)
Number of elements	17	15		
Spacing [λ]	0.5	0.5		
Aperture [λ]	8.0	7.0		
$SLL[dB]$	13.03	12.94	13.44	10.60
$FNBW$ [deg]	13.60	15.31	10.80	15.84
$3dB$ Beamwidth [deg]	5.98	6.77	4.71	7.53
Matching Error, ξ (w.r.t. virtual, outside lens)	-	4.60×10^{-1}	5.19×10^{-1}	6.52×10^{-1}

Table IV: Final summary.

4 Test Case # 2 - Cosine Profile, $N = 15$, $N' = 19$

4.1 Step 1: Expanding the physical array ($N = 15$, $L = 7.0$ [λ])

Input Parameters

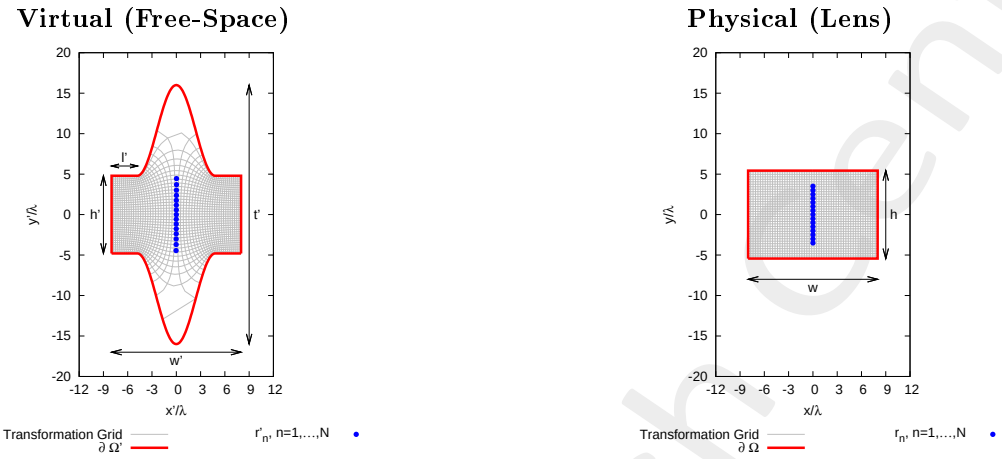

(a) (b)

Figure 13: Transformation regions.

- **Physical Array**
  - Number of elements, spacing, aperture: $N = 15$, $d = \frac{\lambda}{2}$, $L = 7.0$ [λ];
  - Positions: $x_n = 0.0$, $y_n \in [-L/2, L/2]$, $n = 1, ..., N$;
  - Steering angle: $\phi_s = 0.0$ [deg];
  - Excitations: $I_n = 1.0$, $\varphi_n = \frac{-2\pi}{\lambda} y_n sin\,(\phi_s)$; $n = 1, ..., N$;
- **Virtual Geometry (BEKELE)**
  - Dimensions: $w' = 0.5t' = 16.0$ [λ], $h' = 0.3t' = 9.6$ [λ], $t' = 32.0$ [λ], $l' = \frac{w'}{5} = 3.2$ [λ];
- **QCTO**
  - Discretization cell dimension: 0.15 [λ] (0.01 [λ] for source mapping);

4.1.1 Results

- Aperture of the virtual array: $L' \simeq 8.89$ [λ];
- Number of equi-spaced elements in L': $N' = round\left(\frac{L'}{0.5} + 1\right) = 19$;

4.2 Step 2: Compressing the virtual array ($N' = 19$, $L' = 9.0$ [λ])

Input Parameters

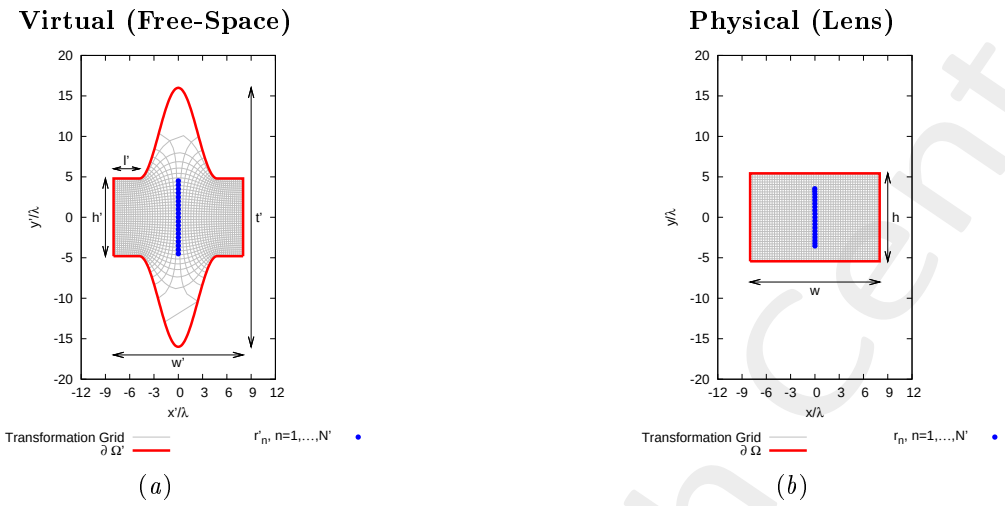

(a) (b)

Figure 14: Transformation regions.

- **Virtual Array**
  - Number of elements, spacing, aperture: $N' = 19$, $d' = \frac{\lambda}{2}$, $L' = 9.0$ [λ];
  - Positions: $x'_n = 0.0$, $y'_n \in [-L'/2, L'/2]$, $n = 1, ..., N'$;
  - Steering angle: $\phi_s = 0.0$ [deg];
  - Excitations: $I'_n = 1.0$, $\varphi'_n = \frac{-2\pi}{\lambda} y_n sin(\phi_s)$; $n = 1, ..., N'$;
  - Operating frequency: $f = 600$ [MHz];
- **Virtual Geometry:** same of step 1;
- **QCTO:** same of step 1;

4.2.1 Results of the Transformation

Lens Permittivity

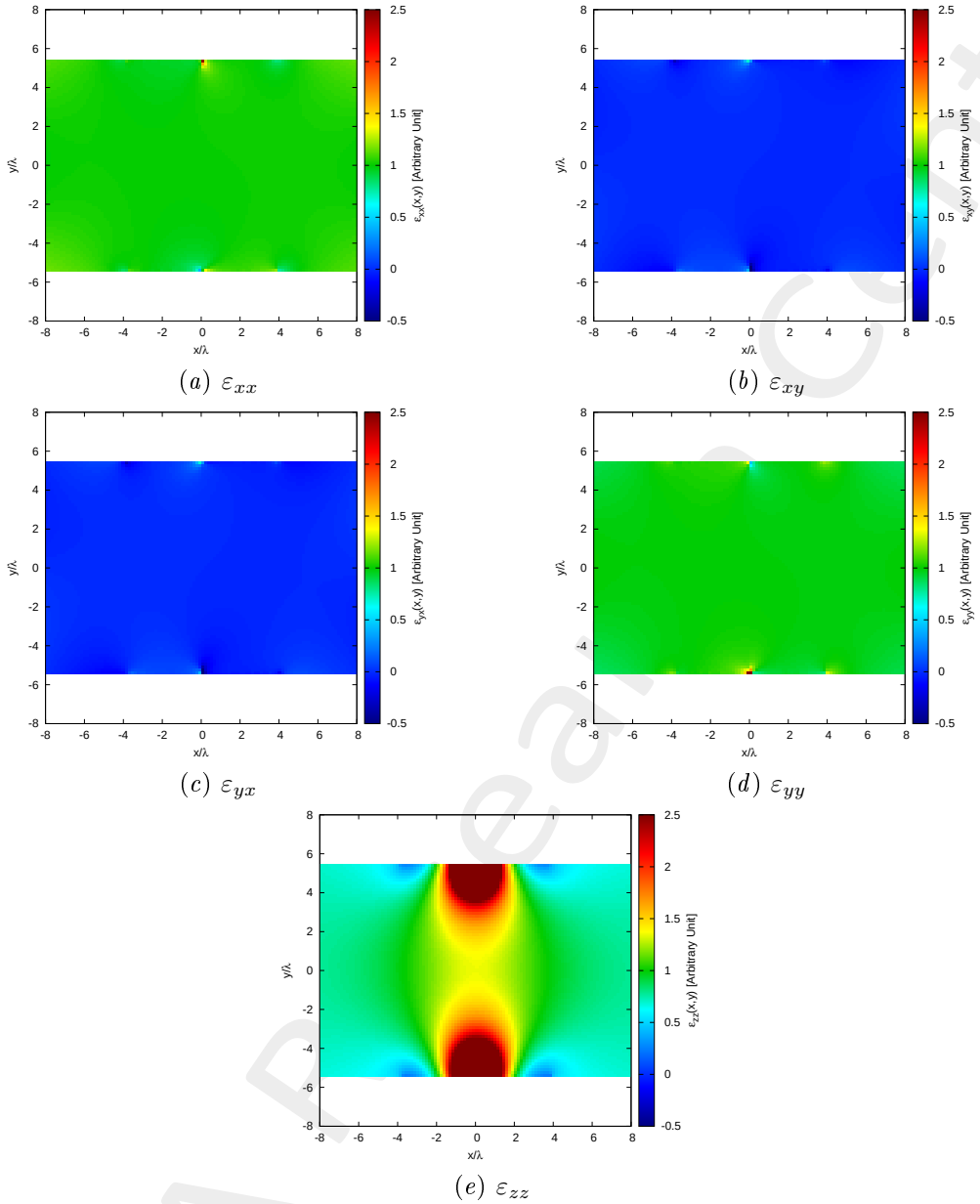

(a) ε_{xx} (b) ε_{xy}

(c) ε_{yx} (d) ε_{yy}

(e) ε_{zz}

Figure 15: Components of the relative permittivity tensor of the lens.

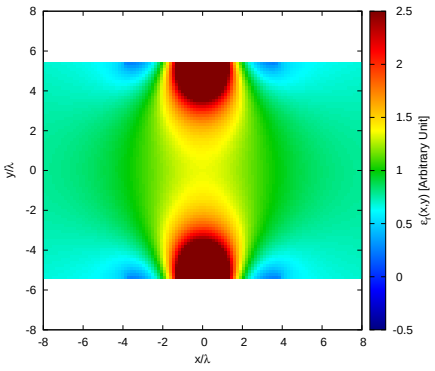

Figure 16: Isotropic approximate permittivity distribution of the lens.

Physical Lens Parameters

Parameter	Value
Height, h $[\lambda]$	10.86
Width, w $[\lambda]$	16.0
Anisotropic Permittivity Range	$[-1.31, 379.05]$
Isotropic Permittivity Range	$[0.00, 242.40]$

Table V: Transformation statistics. Note that we impose $w = w'$, while h' is internally chosen.

Virtual Grid Orthogonality

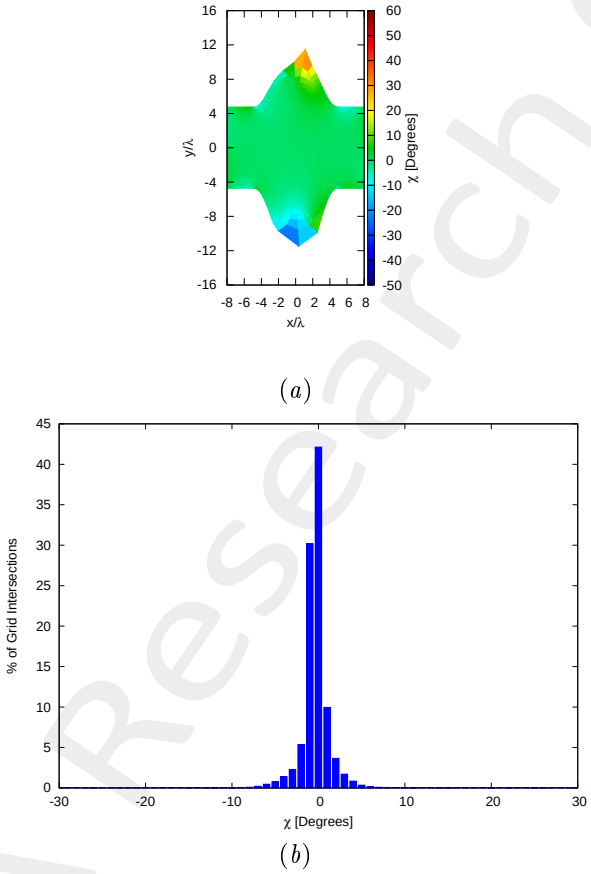

(a)

(b)

Figure 17: Orthogonality of the virtual region.

4.2.2 Near-Field Distributions ($\phi_s = 0$ [deg], $f = 600$ [MHz])

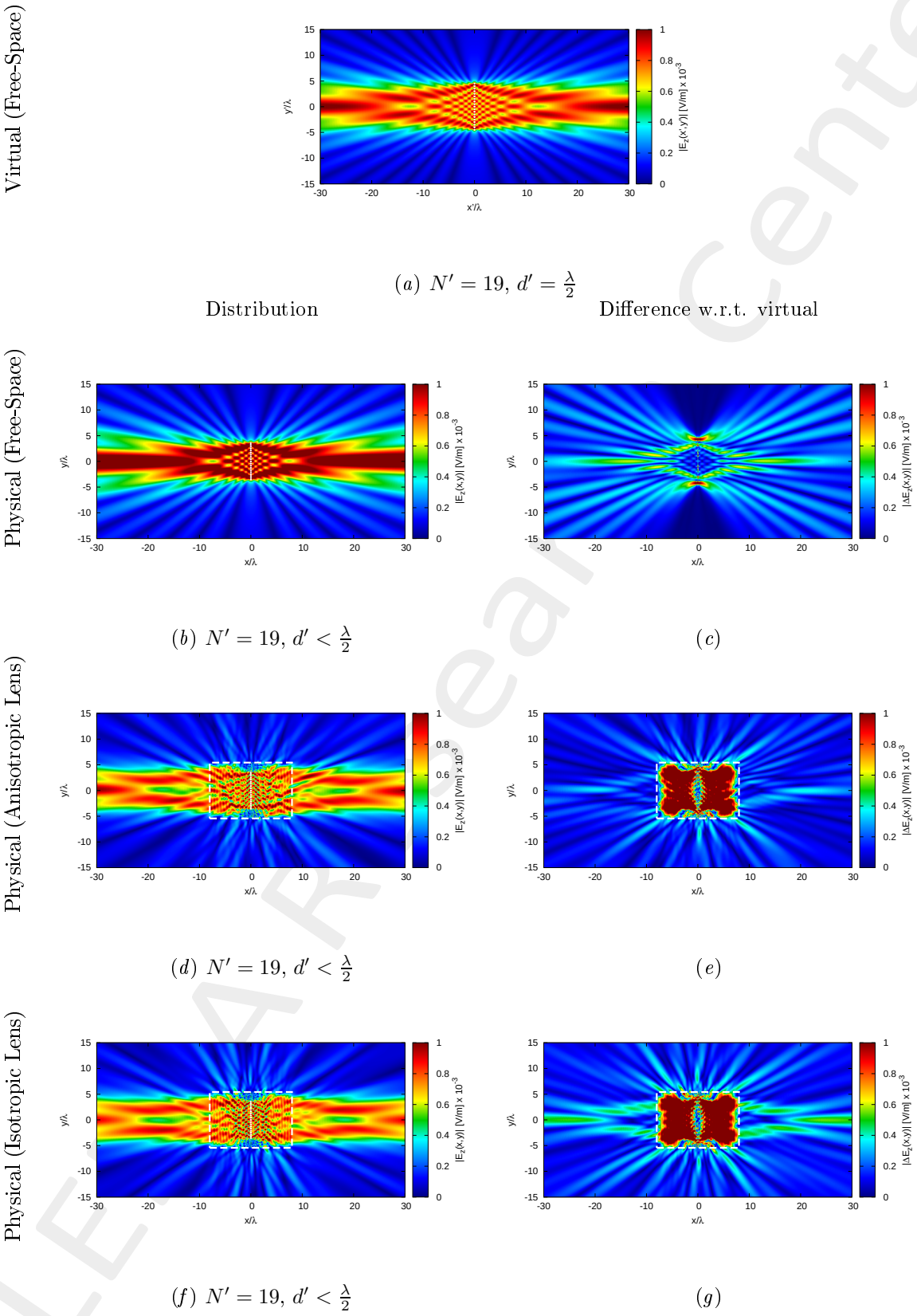

(a) $N' = 19$, $d' = \frac{\lambda}{2}$

(b) $N' = 19$, $d' < \frac{\lambda}{2}$ (c)

(d) $N' = 19$, $d' < \frac{\lambda}{2}$ (e)

(f) $N' = 19$, $d' < \frac{\lambda}{2}$ (g)

Figure 18: Electric field distributions.

4.2.3 Far-Field Patterns ($\phi_s = 0$ [deg], $f = 600$ [MHz])

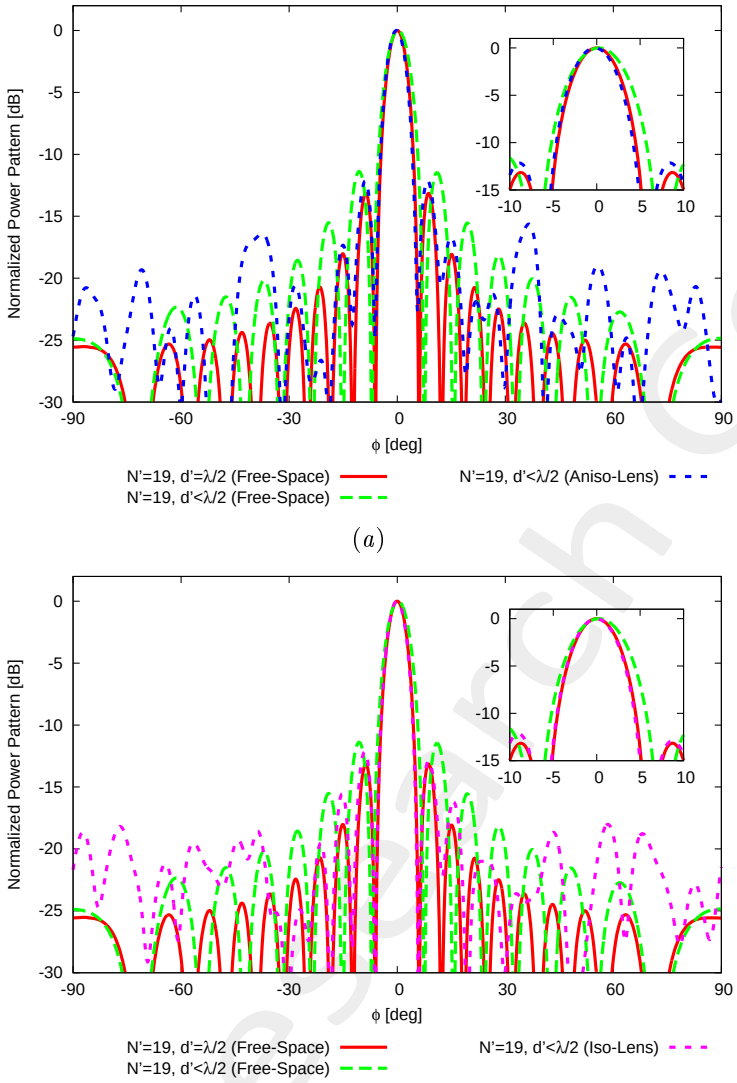

Figure 19: Comparison between normalized power patterns.

4.2.4 Summary ($\phi_s = 0$ [deg], $f = 600$ [MHz])

	Virtual Array	**Physical Array**		
Environment	Free-Space	Free-Space	Aniso-Lens	Iso-Lens
Number of elements	19	19		
Spacing [λ]	0.5	< 0.5		
Aperture [λ]	9.0	7.06		
$SLL[dB]$	13.15	11.40	12.14	12.15
$FNBW$ [deg]	12.16	14.59	11.89	12.07
$3dB$ Beamwidth [deg]	5.37	6.56	5.28	5.32
Matching Error, ξ (w.r.t. virtual, outside lens)	-	6.77×10^{-1}	4.96×10^{-1}	6.70×10^{-1}

Table VI: Summary.

4.3 Source Inversion (SI)

Parameters

- Before SI
  - Number of elements: $N' = 19$, $d' < \lambda/2$;
- After SI
  - Number of elements after SI: $N = 15$, $d = \frac{\lambda}{2}$;
  - Aperture: $L = 7.0$;
- Radius of the observation domain: $r_{SI} = 20.0$ $[\lambda]$;
- Number of field sampling points: $n_{SI} = 1000$.

4.3.1 Results of the SI

Synthesized Excitations ($\phi_s = 0$ [deg], $f = 600$ [MHz])

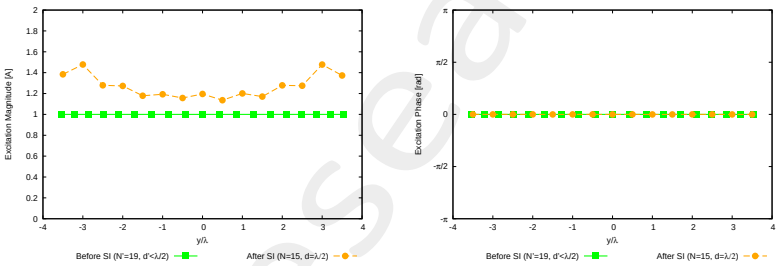

(a) (b)

Figure 20: Excitations of the array ($N = 15$, $d = \frac{\lambda}{2}$) before and after SI.

Check SI: Free-Space Patterns ($\phi_s = 0$ [deg], $f = 600$ [MHz])

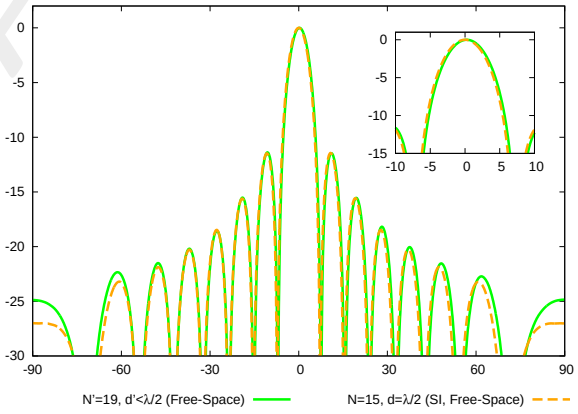

Figure 21: Free-space patterns of reference array and synthesized array after SI.

4.3.2 Near-Field Distribution ($\phi_s = 0$ [deg], $f = 600$ [MHz])

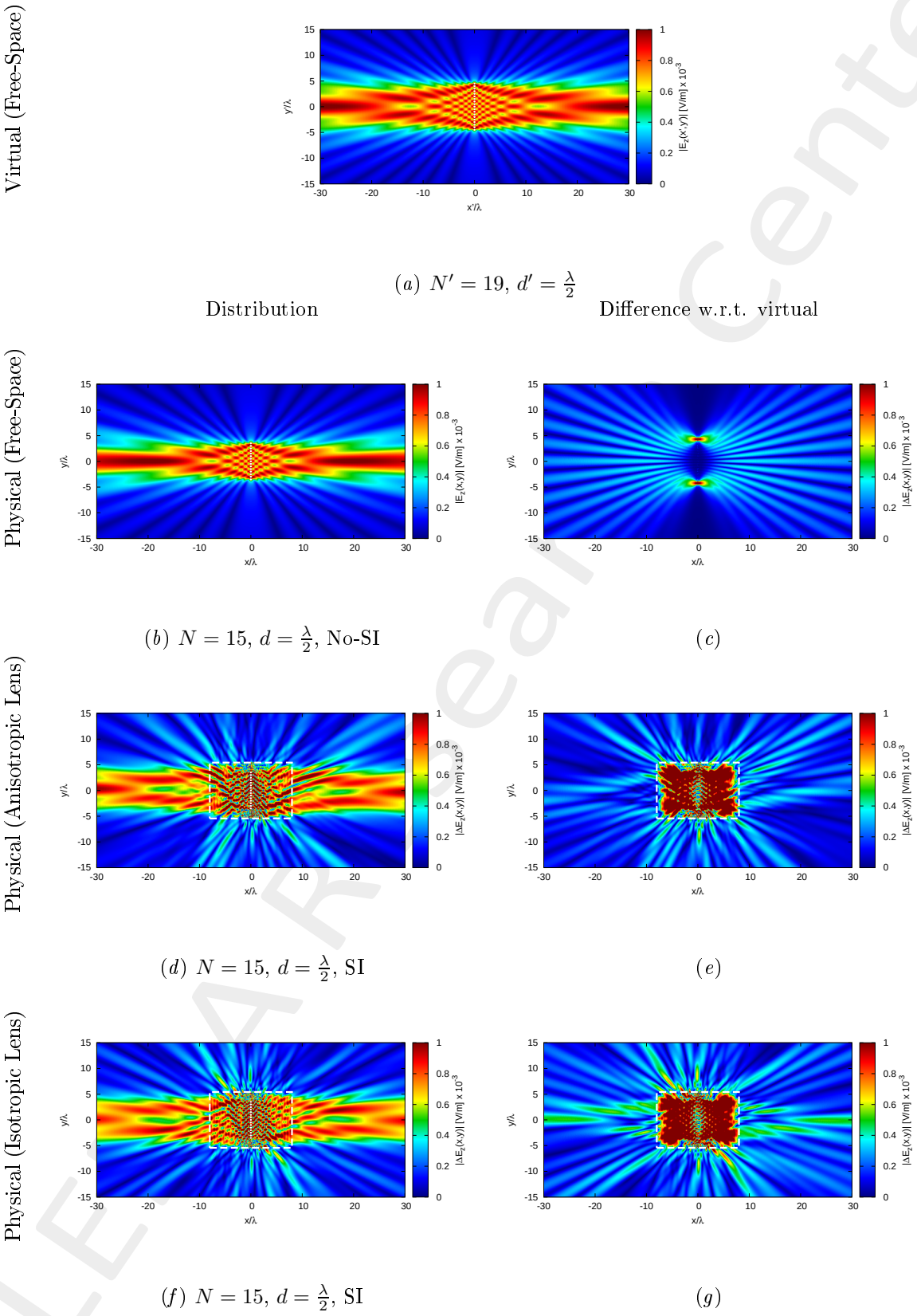

(a) $N' = 19$, $d' = \frac{\lambda}{2}$

(b) $N = 15$, $d = \frac{\lambda}{2}$, No-SI (c)

(d) $N = 15$, $d = \frac{\lambda}{2}$, SI (e)

(f) $N = 15$, $d = \frac{\lambda}{2}$, SI (g)

Figure 22: Electric field distributions.

4.3.3 Far-Field Patterns ($\phi_s = 0$ [deg], $f = 600$ [MHz])

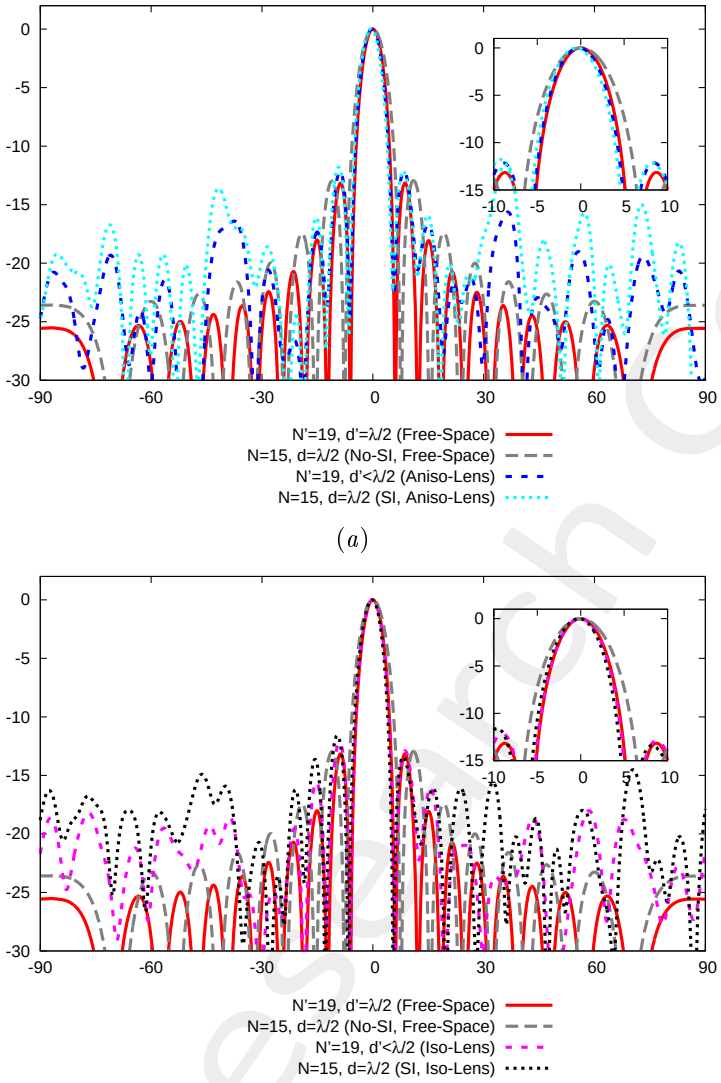

Figure 23: Comparison between normalized power patterns.

4.3.4 Final Summary ($\phi_s = 0$ [deg], $f = 600$ [MHz])

	Virtual Array	**Physical Array**		
Environment	Free-Space	Free-Space (No-SI)	Aniso-Lens (SI)	Iso-Lens (SI)
Number of elements	19	15		
Spacing [λ]	0.5	0.5		
Aperture [λ]	9.0	7.0		
$SLL[dB]$	13.15	12.94	11.45	11.59
$FNBW$ [deg]	12.16	15.31	11.89	12.16
$3dB$ Beamwidth [deg]	5.37	6.77	5.29	5.29
Matching Error, ξ (w.r.t. virtual, outside lens)	-	5.85×10^{-1}	6.08×10^{-1}	7.83×10^{-1}

Table VII: Final summary.

4.3.5 Observations

- Using the lens (both anisotropic and isotropic) the $FNBW$ and $3dB$ BW are reduced for the physical array. However, the SLL is increased;
- With respect to the previous test case (triangular virtual geometry) in this case we can observe a better matching between the anisotropic and isotropic lenses. This is motivated by an higher orthogonality of the virtual region.

References

[1] G. Oliveri, G. Gottardi, F. Robol, A. Polo, L. Poli, M. Salucci, M. Chuan, C. Massagrande, P. Vinetti, M. Mattivi, R. Lombardi, and A. Massa, "Co-design of unconventional array architectures and antenna elements for 5G base station," *IEEE Trans. Antennas Propag.*, vol. 65, no. 12, pp. 6752-6767, Dec. 2017.

[2] P. Rocca, G. Oliveri, R. J. Mailloux, and A. Massa, "Unconventional phased array architectures and design methodologies - A review," *Proc. IEEE*, vol. 104, no. 3, pp. 544-560, Mar. 2016.

[3] G. Oliveri, M. Salucci, N. Anselmi and A. Massa, "Multiscale System-by-Design synthesis of printed WAIMs for waveguide array enhancement," *IEEE J. Multiscale Multiphysics Computat. Techn.*, vol. 2, pp. 84-96, 2017.

[4] A. Massa and G. Oliveri, "Metamaterial-by-Design: Theory, methods, and applications to communications and sensing - Editorial," *EPJ Applied Metamaterials*, vol. 3, no. E1, pp. 1-3, 2016.

[5] L. Poli, G. Oliveri, P. Rocca, M. Salucci, and A. Massa, "Long-Distance WPT Unconventional Arrays Synthesis," *J. Electromagnet. Wave.*, vol. 31, no. 14, pp. 1399-1420, Jul. 2017.

[6] G. Oliveri, F. Viani, N. Anselmi, and A. Massa, "Synthesis of multi-layer WAIM coatings for planar phased arrays within the system-by-design framework," *IEEE Trans. Antennas Propag.*, vol. 63, no. 6, pp. 2482-2496, Jun. 2015.

[7] G. Oliveri, L. Tenuti, E. Bekele, M. Carlin, and A. Massa, "An SbD-QCTO approach to the synthesis of isotropic metamaterial lenses," *IEEE Antennas Wireless Propag. Lett.*, vol. 13, pp. 1783-1786, 2014.

[8] G. Oliveri, D. H. Werner, and A. Massa, "Reconfigurable electromagnetics through metamaterials - A review" *Proc. IEEE*, vol. 103, no. 7, pp. 1034-1056, Jul. 2015.

[9] G. Oliveri, E. T. Bekele, M. Salucci, and A. Massa, "Transformation electromagnetics miniaturization of sectoral and conical horn antennas," *IEEE Trans. Antennas Propag.*, vol. 64, no. 4, pp. 1508-1513, Apr. 2016.

[10] G. Oliveri, E. T. Bekele, M. Salucci, and A. Massa, "Array miniaturization through QCTO-SI metamaterial radomes," *IEEE Trans. Antennas Propag.*, vol. 63, no. 8, pp. 3465-3476, Aug. 2015.

[11] G. Oliveri, E. T. Bekele, D. H. Werner, J. P. Turpin, and A. Massa, "Generalized QCTO for metamaterial-lens-coated conformal arrays," *IEEE Trans. Antennas Propag.*, vol. 62, no. 8, pp 4089-4095, Aug. 2014.

[12] G. Oliveri, E. Bekele, M. Carlin, L. Tenuti, J. Turpin, D. H. Werner, and A. Massa, "Extended QCTO for innovative antenna system designs," IEEE Antenna Conference on Antenna Measurements and Applications (CAMA 2014), pp. 1-3, Nov. 16-19, 2014.

[13] G. Oliveri, P. Rocca, M. Salucci, E. T. Bekele, D. H. Werner, and A. Massa, "Design and synthesis of innovative metamaterial-enhanced arrays," IEEE International Symposium on Antennas Propag. (APS/URSI 2013), Orlando, Florida, USA, pp. 972 - 973, Jul. 7-12, 2013.

[14] G. Oliveri, "Improving the reliability of frequency domain simulators in the presence of homogeneous metamaterials - A preliminary numerical assessment," *Progress In Electromagnetics Research*, vol. 122, pp. 497-518, 2012.

[15] M. Salucci, G. Oliveri, N. Anselmi, G. Gottardi, and A. Massa, "Performance enhancement of linear active electronically-scanned arrays by means of MbD-synthesized metalenses," *J. Electromagnet. Wave.*, vol. 0, no. 0, pp. 1-29, 2017 (DOI: 10.1080/09205071.2017.1410077).